Buoyancy of volatile-rich kimberlite melts, magma ascent, and xenolith transport

Ana Anzulović*[a], Anne H. Davis [a], Carmen Gaina [a], Razvan Caracas [a,b,c]

[a] *Centre for Planetary Habitability, University of Oslo, 0315 Oslo, Norway*

[b] *Institut de Physique du Globe de Paris, CNRS, Université Paris Cité, 75238 Paris, France*

[c] *ICUB, University of Bucharest, 050663, Bucharest, Romania*

*Corresponding author: anzulovicana@gmail.com

Buoyancy of volatile-rich kimberlite melts, magma ascent, and xenolith transport

Ana Anzulović [a,*], **Anne H. Davis** [a], **Carmen Gaina** [a], **Razvan Caracas** [a,b,c]

[a] *Centre for Planetary Habitability, University of Oslo, 0315 Oslo, Norway*

[b] *Institut de Physique du Globe de Paris, CNRS, Université Paris Cité, 75238 Paris, France*

[c] *ICUB, University of Bucharest, 050663, Bucharest, Romania*

ABSTRACT

Kimberlite melts are primary carriers of mantle-derived carbon and hydrogen, playing an important role in Earth's deep carbon cycle and diamond transport. Their low densities, viscosities, and vapor exsolution enable fast ascent rates. Ascending from the upper mantle, kimberlite melts incorporate xenoliths and xenocrysts and exsolve volatiles. These processes alter their initial composition, increasing the discrepancy between the proto-kimberlite magma and the magma that reaches the surface. To explain kimberlite volcanism, we examine atomic diffusivities and densities of kimberlite melts with varying volatile contents. We show that water makes the melts more diffusive, which should also lower their viscosity. All our kimberlite melts are positively buoyant below the lower continental crust (the MOHO discontinuity). They require ~8.2 wt% CO_2 to cross and rise through the MOHO. Above the MOHO, the most volatile-rich kimberlite melts can carry up to ~44% xenolithic fragments of depleted peridotite type.

Keywords: kimberlite melt, carbon, density, diffusivity, EOS

INTRODUCTION

Kimberlites are volatile-rich, low-density melts that originate from the subcratonic mantle. Kimberlite volcanism clusters in time and space, and is mostly restricted to Archaean cratons and their associated subcontinental lithosphere (Dawson, 1971; Torsvik et al., 2010).

The rapid ascent of kimberlites ensures the preservation and transportation of mantle-derived xenoliths to Earth's surface. This ascent is related to their low viscosity and low density. In a melt, atomic diffusivity influences the viscosity and also controls the chemical homogenization rate, bubble formation and dynamics (Sparks, 1978; Watson, 1982), crystal dissolution, and mixing. While atomic diffusion in silicate melts has been well studied (Zhang et al., 2010), the extent to which the presence of volatiles, like carbon and hydrogen, enhance the diffusivities of other atomic species is unclear. Previous studies showed that H_2O disrupts the silicate network by breaking bridging oxygen bonds and enhancing atomic diffusion (Le Losq et al., 2015; Zhang et al., 2010). CO_2 diffuses slower than H_2O in depolymerized melts, leading to volatile fractionation during magma ascent (Zhang et al., 2010). The effect of carbon is variable and depends on the composition of the silicate melt (Ghosh & Karki, 2017; Solomatova et al., 2020; Vuilleumier et al., 2015). Besides composition, atomic diffusivities also depend on temperature, pressure, and oxygen fugacity (Zhang et al., 2010). Understanding how atomic diffusivity is affected by these changing parameters is key to understanding kimberlite ascent, as this controls element transport and reaction kinetics.

Melt density is another key parameter in understanding ascent, as it governs buoyancy and ascent rates. The density of a melt relative to its surroundings determines if it stalls, sinks, or rises. Kimberlites originate from a metasomatized mantle domain, carbon-enriched relative to the depleted cratonic lithosphere (Stamm & Schmidt, 2017). Their buoyancy is largely controlled by carbon content, which influences melt density and volatile exsolution. Previous studies have suggested a wide range of CO_2 concentrations (7-14 wt%) (Giuliani et al., 2023), but

the threshold required for successful ascent remains unclear.

To address how atomic diffusivity and density affect kimberlite ascent we use the Jericho kimberlite melt of the Slave craton (Northwest Territories and Nunavut, Canada; Fig. 1A) as a model. Its geological context is illustrated in a cross-sectional view of the Slave craton that highlights the lithospheric structure and the Jericho drill site (Nunavut; Fig. 1B). The geochemistry of the estimated parental magmas was thoroughly characterized in previous studies (Kopylova et al., 2007, and references therein). Using *ab initio* molecular dynamics (AIMD), we calculated the atomic self-diffusion and densities of these kimberlite melts. We estimated their buoyancy relative to the Slave craton and estimated their capacity to transport depleted peridotite (DPer) xenoliths.

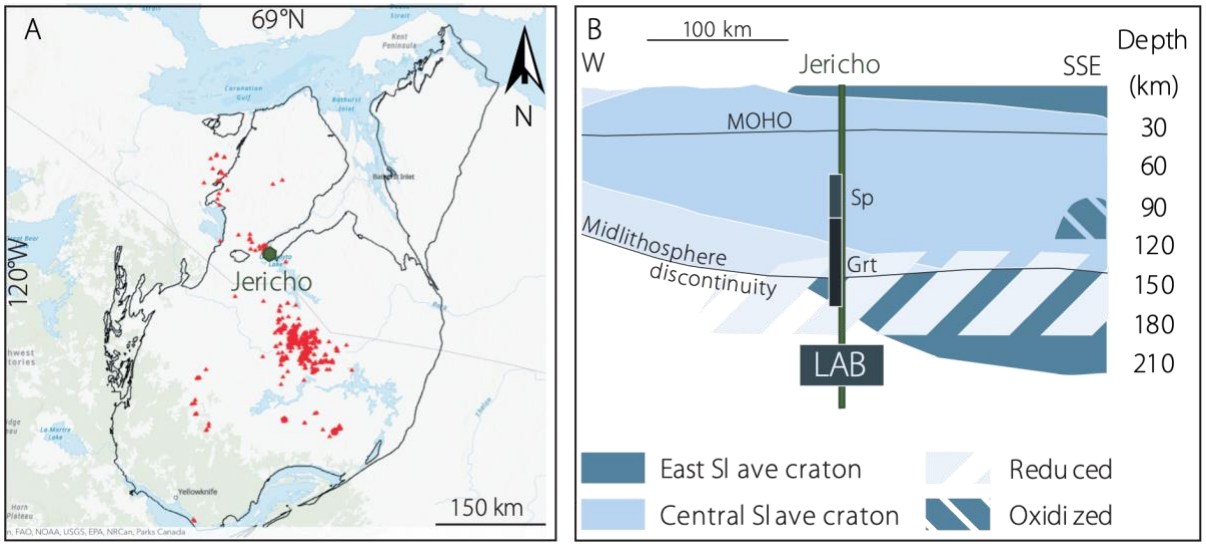

Figure 1: Geological setting of the Jericho kimberlite. (A) Map of the Slave craton (outlined in black), showing the location of the Jericho kimberlite pipe (green hexagon) relative to other known kimberlite occurrences (red triangles) (Northwest Territories and Nunavut, Canada; Stubley and Irwin, 2019). (B) Cross-section of the Slave craton in proximity of the Jericho kimberlite. The model highlights distinct domains of the Central and East Slave craton and zones with varying redox states (after Snyder et al., 2014). Dark-blue and black rectangles indicate mantle layers characterized by spinel- and garnet-facies peridotites, respectively, based on compositional distinctions from xenolith studies (Snyder et al., 2014 and references therein). MOHO—Mohorovičić discontinuity; Sp—spinel; Grt—garnet; LAB—lithosphere-asthenosphere boundary.

METHODS

We employed the Vienna Ab Initio Simulation Package (https://www.vasp.at; Kresse & Furthmüller, 1996) to perform the AIMD simulations, and used the projector augmented wave method (Blöchl, 1994) of the density functional theory. We used the generalized gradient approximation (Perdew et al., 1996) for the exchange-correlation. The plane-waves kinetic energy cutoff was 600 eV and the cutoff for augmentation charges was 800 eV. We reached convergence of the internal energy to better than 15 meV/atom. We employed the NVT canonical ensemble with constant number of atoms (N), volume (V), and temperature (T), controlled by a Nosé-Hoover thermostat. The timestep was 1 fs, and after a discarded 500 fs thermalization period the production runs lasted between 3 and 60 ps. The simulations were performed at 1500, 2000, 2500, and 3000 K, over a wide pressure range to improve the equation of state fits.

We used a composition (Table S1 in the Supplemental Material[1]) based on the hypabyssal Jericho kimberlite, from which the proto-kimberlite melt was reconstructed before assimilation of orthopyroxene (Kopylova et al., 2007). We constructed a dry kimberlite melt (DK) devoid of volatiles with stoichiometry $Mg_{52}Si_{33}Ca_{17}Fe_8Ti_2Al_1K_1O_{151}$, using a cubic supercell of 265 atoms. This represents a commonly accepted cell size for AIMD simulations that balances computational feasibility and statistical robustness. Our theoretical composition approximates the analytical values within 1 oxide wt%. We developed additional compositions by incorporating H_2O and CO_2 into the thermalized DK:

- carbon-poor kimberlite melt (CPK) = DK + 8 CO_2 (5.6 wt% CO_2)
- carbon-rich kimberlite melt (CRK) = DK + 17 CO_2 (11.3 wt% CO_2)
- water-poor kimberlite melt (WPK) = CRK + 8 H_2O (11.3 wt% CO_2, 2.2 wt% H_2O)
- water-rich kimberlite melt (WRK) = CRK + 38 H_2O (11.3 wt% CO_2, 9.3 wt% H_2O)

We analyzed the results of the simulations with the UMD package (Caracas et al., 2021). Further details are given in the Supplemental Material.

RESULTS AND DISCUSSION

Element mobility expressed by the self-diffusion coefficient is a proxy for transport properties of a melt. The slowest diffusing elements determine global transport characteristics. Si is the least diffusing species (Fig. 2) due to strong Si-O covalent bonds, which result in long-lived SiOx coordination polyhedra, that are further polymerized and form the backbone of the melt. Oxygen diffuses faster than Si, as do potassium and Ca, which act as network modifiers. After hydrogen, Mg and Fe are the fastest-diffusing species in the melt. The hydrogen diffusion rate in the melt is comparable to that of carbon in the vapor.

Above 3 GPa, Si and carbon diffuse at about the same rate (Fig. 2), due to their structural similarities. Below 3 GPa, carbon diffusivity rises by ~0.7 orders of magnitude, twice the increase observed for Si (~0.3 orders of magnitude) (Fig. 2). This increase occurs as CO and CO_2 molecules appear, triggering nucleation of carbon-rich nanobubbles (Davis & Caracas, 2024; Moussallam et al., 2016; Solomatova & Caracas, 2021), where vapor species diffuse freely. The nucleation of a gas phase below 3 GPa provides an additional buoyant force that accelerates the kimberlite ascent.

Adding carbon has virtually no effect on diffusion rates of other elements, consistent with findings for other carbon-bearing silicate melts (Davis et al., 2023; Solomatova et al., 2020; Vuilleumier et al., 2015) (Fig. 2). In contrast, hydrogen addition increases atomic diffusion of other elements by up to half an order of magnitude, likely due to its depolymerizing effect on the silicate network (Moussallam et al., 2016; Pöhlmann et al., 2004). An increase in H_2O content from 2.2 wt% to 9.3 wt% does not alter diffusivity.

The diffusion rates reflect local scale melt homogenization and can be related to viscosity. Viscosity is too computationally costly to calculate, but we can estimate the relative effects of volatiles. The depolymerized structure of DK melts already makes viscosity extremely low, up

to two orders of magnitude lower than that of basalts (Hao et al., 2024). Our simulations suggest that carbon has no measurable impact, but H_2O increases diffusion by approximately one order of magnitude, likely reducing the viscosity. Such hydrous kimberlite melts are extremely mobile in the crust.

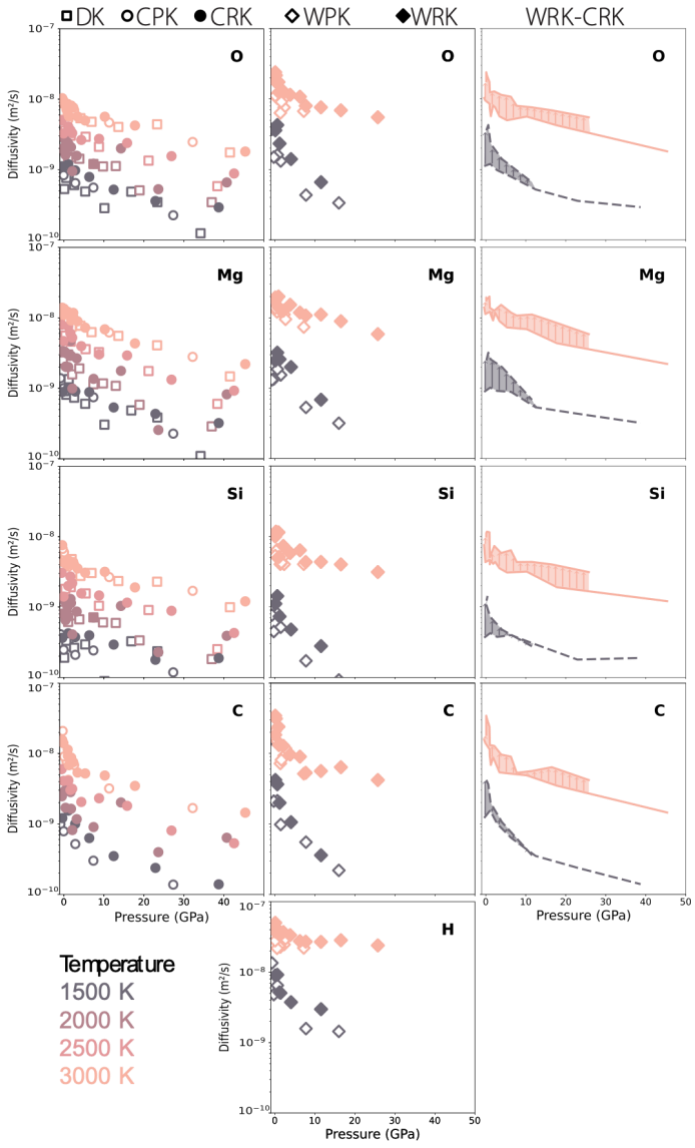

Figure 2: Self-diffusion coefficients of major elements in kimberlite melts. Plots show self-diffusion coefficients versus pressure for key elements (oxygen, Mg, Si, carbon, hydrogen) in five different kimberlite melt compositions. Each row corresponds to an element, and columns group different melt types. Diffusivity decreases with increasing pressure and decreasing temperature (indicated by color). The DK, CPK, and CRK melts exhibit comparable diffusivities, while hydrous compositions (WPK and WRK) show significantly higher values than anhydrous melts. This effect is illustrated in the rightmost column, which explicitly compares water-rich (WRK) and carbon-rich (CRK) melts, highlighting the pronounced increase in diffusivity caused by water. Abbreviations: DK—dry kimberlite; CPK—

carbon-poor kimberlite; CRK—carbon-rich kimberlite; WPK—water-poor kimberlite; WRK—water-rich kimberlite.

Table 1: Equation of states parameters for the simulated kimberlite melts.

Composition	ρ_0 (g/cm^3)	K_0 (GPa)	K'
T = 1500 K			
DK	2.62	23	5.6
CPK	2.5	19	6.1
CRK	2.4	16	6.2
WPK	2.09	10	9.8
WRK	2.02	10.3	5.7
T = 2000 K			
DK	2.52	21	5.5
CRK	2.32	16	5.9
T = 2500 K			
DK	2.47	24	4.6
CRK	2.15	19	5.7
T = 3000 K			
DK	2.35	21	4.7
CPK	2.15	10	6.2
CRK	2.06	9	6.3
WPK	1.77	10	5.7
WRK	1.42	18	5.7

Note: Zero-pressure density (ρ_0), bulk modulus (K_0), and the first derivative of the bulk modulus (K') are obtained from the third-order Birch Murnaghan equation of state fit to isothermal pressure–volume data. The individual parameters show some non-monotonic variation with temperature (T) due to independent fitting of data at each isotherm, variations in the fitting range, thermal expansion, sluggishness at low T, etc. DK—dry kimberlite; CPK—carbon-poor kimberlite; CRK—carbon-rich kimberlite; WPK—water-poor kimberlite; WRK—water-rich kimberlite.

The most intriguing aspect of kimberlites is their density, significantly lower than that of

other primitive melts in Earth's upper mantle. We fit a third-order Birch-Murnaghan equation of state to pressure density data (Table 1). Figure 3A shows the resulting profiles at 1500 K and Figure S4 shows the remaining isotherms. The density decrease from added volatiles correlates with both their concentration and type (Fig. 3B). The trends are similar to those observed in pyrolite melts (Solomatova & Caracas, 2019).

All melts are most compressible between 0 and 1 GPa where structural rearrangements cause significant packing changes. Melt compressibility is directly related to the concentration of volatiles. At 1500 K, DK has a bulk modulus of 23 GPa, decreasing with CO_2 addition to 19 GPa in CPK and 16 GPa in CRK, and to 10 GPa in WPK and WRK (Table 1). H_2O affects compressibility more than carbon by depolymerizing the melt network and acting as a network modifier, which allows its compression behavior to be decoupled from that of the silicate network (Ritter et al., 2020).

To further illustrate the effects of CO_2 and H_2O on melt density, we subtracted volatile-bearing melt density profiles from that of DK (Fig. 3B). More-negative values indicate higher buoyancy compared to the DK. CO_2-bearing melts exhibit constant density reduction across all calculated pressures with minimal variation in the relative density profile as pressures increase. In contrast, density reduction in H_2O-bearing melts, derived from both H_2O and CO_2, is more pronounced between 0 and 1 GPa compared to higher pressures. As pressure increases, this density reduction plateaus, as the high compressibility of hydrous melts makes the water effect less important at high pressures (Jing & Karato, 2012). This highlights the importance of water in the last stage of ascent, as it amplifies melt's positive buoyancy relative to crust.

To contextualize this, we compared densities of kimberlite melt to the density of the surrounding lithosphere. Figure 3A shows the density profile of the Preliminary Reference Earth Model (PREM) (Dziewonski & Anderson, 1981) and the Slave craton (Snyder, 2008). Snyder (2008) identified seismic discontinuities within the Slave craton, including MOHO (the discontinuity between the crust and the mantle) at 38 km depth, the base of an ultradepleted

layer at 145 km, and the lithosphere-asthenosphere boundary between 190 and 220 km (Fig. 1B).

Above 1.2 GPa all kimberlites have lower densities than the Slave craton, and in a simplified assumption they should buoyantly rise (Fig. 3C). Below 1.2 GPa, in the upper 38 km, DK is denser than the cratonic lithosphere (Fig. 3C). CPK is also denser than the Slave craton at MOHO, which would prevent upward migration across this boundary layer. As illustrated in Figure 3C, at least 8.2 wt% CO_2 (assuming no water) is needed to maintain buoyancy across the MOHO. However, the more volatile-rich compositions (i.e. CRK, WPK, and WRK) remain buoyant throughout their entire ascent across the MOHO and through the crust.

The low densities of volatile-rich kimberlite melts allow for efficient upward entrainment and transportation of dense xenoliths and xenocrysts. To estimate the quantity of entrained fragments that kimberlite melts might transport, we add DPer (Faccincani et al., 2021) and calculate the maximum percentage of fragments that can be carried while maintaining neutral buoyancy (see the Supplemental Material for details). The CRK can incorporate up to 21% DPer at 0 GPa and 1500 K (Fig. 3D). Under the same conditions, WPK, and WRK compositions can incorporate 31% and 44% DPer, respectively. There is a 9% increase in DPer amount that can be carried by going from CPK to CRK, and a 24% increase when comparing CRK to WRK. These estimates agree with observations of volumetric proportion of mantle-derived olivine xenocrysts, typically accounting for ~20% to 30% of the total magma volume (Brett et al., 2009; Soltys et al., 2018). We find that in our most volatile-rich composition, kimberlites can carry up to 44% of fragments.

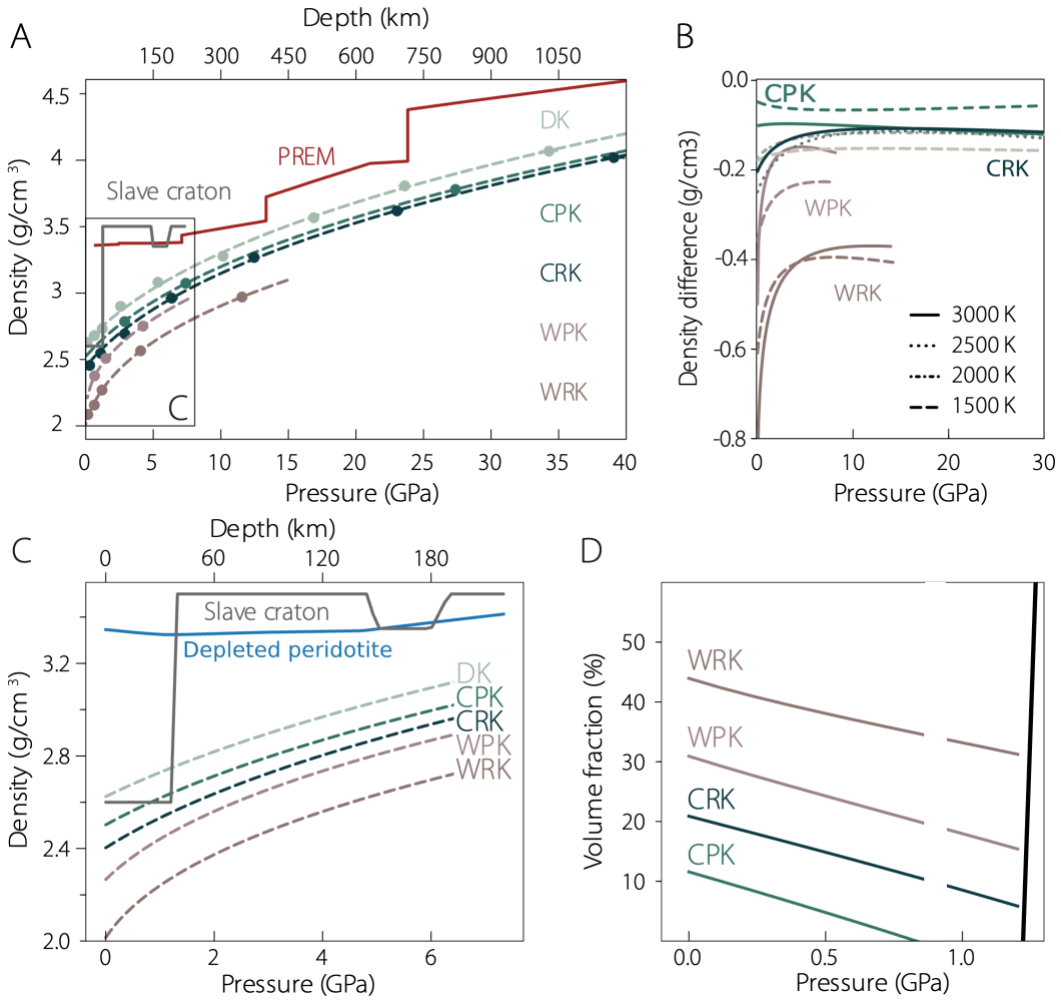

Figure 3: Density, buoyancy, and transport capacity of kimberlite melts. (A) Absolute densities of kimberlite compositions. Dashed lines are Birch-Murnaghan equations of state fits at 1500 K. The densities are compared to the Preliminary Reference Earth Model (PREM) (Dziewonski and Anderson, 1981) and the Slave craton (Canada; Snyder, 2008). DK—dry kimberlite; CPK—carbon-poor kimberlite; CRK—carbon-rich 358 kimberlite; WPK—water-poor kimberlite; WRK—water-rich kimberlite. (B) Changes in the density of the liquids compared to the dry kimberlites due to the addition of volatiles. This highlights the greater efficiency of water over carbon in reducing melt density, especially at lower pressures. (C) Zoomed-in inset from panel A, showing that densities of the DK and the CPK are higher than that of kimberlite from the Slave craton, causing them to stagnate in the last 38 km of the lithosphere. (D) Maximum volume fraction of entrained peridotite fragments for different kimberlite melts at 1500 K during shallow ascent (0–1.27 GPa).

Our model simplifies kimberlite ascent by treating peridotite as inert and assuming a closed system with intact xenolith transport, excluding melt–rock reactions, and xenolith disaggregation. These simplifications help isolate melt properties and generate conservative upper bounds for transport estimates and xenolith cargo. However, in reality, processes like

assimilation of lithospheric mantle components and carbonate breakdown significantly modify melt composition, enhancing CO_2 exsolution and buoyancy at depths greater than 100 km (Brett et al., 2009; Casetta et al., 2023a; 2023b; Russell et al., 2012). The disintegration of peridotite fragments, rather than their transport as intact blocks, increases the surface area available for reaction, further influencing melt properties and the efficiency of xenocryst entrainment. This mechanism is supported at least in the last 120 km of kimberlite ascent (Casetta et al., 2023b). Future models should incorporate dynamic melt–rock interactions and fragment disaggregation to better reflect the evolving physical and chemical state of ascending kimberlite magmas, ultimately improving our understanding of melt mobility and mantle sampling under natural conditions.

CONCLUSIONS

We examined how volatiles influence the atomic diffusivity and density of kimberlite melts as a function of depth, from *ab initio* molecular dynamics. Our results show that Si and other cations have self-diffusion coefficients similar to those in other silicate melts. Carbon has little effect on the diffusion rates of the other atoms, while hydrogen increases their diffusivity by approximately one order of magnitude, through the disruption of the silicate network. This increase in atomic diffusivity would decrease the melt viscosity, enhancing its mobility in the crust and shallow upper mantle. The nucleation of carbon-rich bubbles during decompression below 3 GPa enhances this effect, as it creates a supplementary buoyant force.

The largest ascent driving force is related to the low density of kimberlite melts. We show that below 38 km depth all kimberlite melts are positively buoyant, regardless of their volatile content, and would rise through the surrounding mantle. At low pressures, CO_2 lowers the melt density linearly and H_2O lowers it exponentially. This reduction in density enables positive buoyancy and allows for continued melt ascent. However, some of these melts would remain

stagnant upon reaching the MOHO. Adding volatiles makes kimberlite melts buoyant, with 8.2 wt% CO_2 necessary for nonhydrous melts to cross this boundary below the Slave craton. Above MOHO, volatile-rich kimberlite melts may transport huge amounts of mantle-derived xenoliths and xenocrysts. We find that at 1.2 GPa and 1500 K the most volatile-rich composition can lift up to 44% DPer fragments by volume. This tremendous amount coupled with the computed devolatilization upon ascent is comparable to field observations of kimberlite pipes, where carbon was mostly lost during the explosive eruption and the primordial melt is rich in xenoliths and xenocrysts.

Our study does not aim to capture the full complexity of melt-rock interaction during ascent. Instead, we focus on how volatile content constrains the diffusivity and density of kimberlites. While we do not model xenolith assimilation and disintegration, our results include carbon exsolution at lower pressures. Including assimilation would increase the degree of carbon exsolution, potentially enhancing melt acceleration and buoyancy. Thus, our current approach offers a conservative estimate of the volatile content required for a successful ascent.

ACKNOWLEDGMENTS

We acknowledge support from the CompSci project (EU Horizon 2020, MSCA grant 945371), NFR (Projects 332523 and 325567-HIDDEN), and Sigma2 for simulation resources (grant NN9697K). We thank editor Tracy Rushmer for managing the review process. We are grateful to F. Casetta and two anonymous reviewers for their constructive feedback, which significantly straighten the manuscript.

REFERENCES

Blöchl, P. E., 1994, Projector augmented-wave method. Physical Review: B, v. 50, p. 17,953–227 17,979, https://doi.org/10.1103/PhysRevB.50.17953.

Brett, R. C., Russell, J., & Moss, S., 2009, Origin of olivine in kimberlite: Phenocryst or impostor? Lithos, v. 112, p. 201–212, https://doi.org/10.1016/j.lithos.2009.04.030.

Caracas, R., Kobsch, A., Solomatova, N. V., Li, Z., Soubiran, F., & Hernandez, J.-A., 2021, Analyzing melts and fluids from ab initio molecular dynamics simulations with the UMD package: Journal of Visualized Experiments, v. 175, https://doi.org/10.3791/61534.

Casetta, F., Asenbaum, R., Ashchepkov, I., Abart, R., and Ntaflos, T., 2023a, Mantle-derived cargo vs Liquid line of descent: Reconstructing the P–T–fO2–X path of the Udachnaya–East kimberlite melts during ascent in the Siberian sub-cratonic lithosphere: Journal of Petrology, v. 64, https://doi.org/10.1093/petrology/egac122.

Casetta, F., Asenbaum, R., Ashchepkov, I., Ageeva, O., Abart, R., and Ntaflos, T., 2023b, Ascent rate of the Udachnaya-East kimberlite melts from olivine diffusion chronometry: Earth and Planetary Science Letters, v. 619, https://doi.org/10.1016/j.epsl.2023.118322.

Davis, A.H., and Caracas, R., 2024, Degassing of CO2 triggers large-scale loss of helium from magma oceans: Communications Earth & Environment, v. 5, 344, https://doi.org/10.1038/s43247-024-01509-1.

Davis, A.H., Solomatova, N.V., Caracas, R., and Campbell, A.J., 2023, Carbon storage in Earth's deep interior implied by carbonate-silicate-iron melt miscibility: Geochemistry, Geophysics, Geosystems, v. 24, https://doi.org/10.1029/2023GC010896.

Dawson, J.B., 1971, Advances in kimberlite geology: Earth-Science Reviews, v. 7, p. 187–214, https://doi.org/10.1016/0012-8252(71)90120-6.

Dziewonski, A.M., and Anderson, D.L., 1981, Preliminary reference Earth model: Physics of the Earth and Planetary Interiors, v. 25, p. 297–356, https://doi.org/10.1016/0031-9201(81)90046-7.

Esri, TomTom, G.F.N.U.O., and the GIS User Community, 2025, Slave province NWTOF2019-01 (map). [[See correct citation under Stubley and Irwin.

Faccincani, L., Faccini, B., Casetta, F., Mazzucchelli, M., Nestola, F., and Coltorti, M., 2021, EoS of mantle minerals coupled with composition and thermal state of the lithosphere: Inferring the density structure of peridotitic systems: Lithos, v. 404–405, https://doi.org/10.1016/j.lithos.2021.106483.

Ghosh, D.B., and Karki, B.B., 2017, Transport properties of carbonated silicate melt at high pressure: Science Advances, v. 3, https://doi.org/10.1126/sciadv.1701840.

Giuliani, A., Schmidt, M.W., Torsvik, T.H., and Fedortchouk, Y., 2023, Genesis and evolution of kimberlites: Nature Reviews: Earth & Environment, v. 4, p. 738–753, https://doi.org/10.1038/s43017-023-00481-2.

Hao, M., Zhou, W.-Y., Hrubiak, R., Kenney-Benson, C., Kavanagh, J.L., Davis, W., and Zhang, J.S., 2024, The ultralow viscosity of volatile-rich kimberlite magma: Implications for the water content of primitive kimberlite melts: Science Advances, v. 10, eado8550, https://doi.org/10.1126/sciadv.ado8550.

Jing, Z., and Karato, S., 2012, Effect of H2O on the density of silicate melts at high pressures: Static experiments and the application of a modified hard-sphere model of equation of state: Geochimica et Cosmochimica Acta, v. 85, p. 357–372,

https://doi.org/10.1016/j.gca.2012.03.001.

Kopylova, M., Matveev, S., and Raudsepp, M., 2007, Searching for parental kimberlite melt: Geochimica et Cosmochimica Acta, v. 71, p. 3616–3629, https://doi.org/10.1016/j.gca.2007.05.009.

Kresse, G., and Furthmüller, J., 1996, Efficiency of ab-initio total energy calculations for metals and semiconductors using a plane-wave basis set: Computational Materials Science, v. 6, p. 15–50, https://doi.org/10.1016/0927-0256(96)00008-0.

Le Losq, C., Mysen, B.O., and Cody, G.D., 2015, Water and magmas: Insights about the water solution mechanisms in alkali silicate melts from infrared, Raman, and 29Si solid-state NMR spectroscopies: Progress in Earth and Planetary Science, v. 2, 22, https://doi.org/10.1186/s40645-015-0052-7.

Moussallam, Y., Morizet, Y., and Gaillard, F., 2016, H2O–CO2 solubility in low SiO2-melts and the unique mode of kimberlite degassing and emplacement: Earth and Planetary Science Letters, v. 447, p. 151–160, https://doi.org/10.1016/j.epsl.2016.04.037.

Perdew, J.P., Burke, K., and Ernzerhof, M., 1996, Generalized gradient approximation made simple: Physical Review Letters, v. 77, https://doi.org/10.1103/PhysRevLett.77.3865.

Pöhlmann, M., Benoit, M., and Kob, W., 2004, First-principles molecular-dynamics simulations of a hydrous silica melt: Structural properties and hydrogen diffusion mechanism: Physical Review B: Condensed Matter and Materials Physics, v. 70, https://doi.org/10.1103/PhysRevB.70.184209.

Ritter, X., Sanchez-Valle, C., Sator, N., Desmaele, E., Guignot, N., King, A., Kupenko, I., Berndt, J., and Guillot, B., 2020, Density of hydrous carbonate melts under pressure, compressibility of volatiles and implications for carbonate melt mobility in the upper mantle: Earth and Planetary Science Letters, v. 533, https://doi.org/10.1016/j.epsl.2019.116043.

Russell, J.K., Porritt, L.A., Lavallée, Y., and Dingwell, D.B., 2012, Kimberlite ascent by

assimilation-fuelled buoyancy: Nature, v. 481, p. 352–356, https://doi.org/10.1038/nature10740.

Snyder, D.B., 2008, Stacked uppermost mantle layers within the Slave craton of NW Canada as defined by anisotropic seismic discontinuities: Tectonics, v. 27, TC4006, https://doi.org/10.1029/2007TC002132.

Snyder, D., Hillier, M., Kjarsgaard, B., de Kemp, E., and Craven, J., 2014, Lithospheric architecture of the Slave craton, northwest Canada, as determined from an interdisciplinary 3-D model: Geochemistry, Geophysics, Geosystems, v. 15, p. 1895–1910, https://doi.org/10.1002/2013GC005168.

Solomatova, N.V., and Caracas, R., 2019, Pressure-induced coordination changes in a pyrolitic silicate melt from ab initio molecular dynamics simulations: Journal of Geophysical Research: Solid Earth, v. 124, p. 11,232–11,250, https://doi.org/10.1029/2019JB018238.

Solomatova, N.V., and Caracas, R., 2021, Buoyancy and structure of volatile-rich silicate melts: Journal of Geophysical Research: Solid Earth, v. 126, https://doi.org/10.1029/2020JB021045.

Solomatova, N., Caracas, R., and Cohen, R., 2020, Carbon speciation and solubility in silicate melts, in Manning, C.E., et al., eds., Carbon in Earth's Interior: American Geophysical Union Geophysical Monograph, v. 249, p. 179–194, https://doi.org/10.1002/9781119508229.ch16.

Soltys, A., Giuliani, A., and Phillips, D., 2018, A new approach to reconstructing the composition and evolution of kimberlite melts: A case study of the archetypal Bultfontein kimberlite (Kimberley, South Africa): Lithos, v. 304–307, p. 1–15, https://doi.org/10.1016/j.lithos.2018.01.027.

Sparks, R.S.J., 1978, The dynamics of bubble formation and growth in magmas: A review and analysis: Journal of Volcanology and Geothermal Research, v. 3, p. 1–37, https://doi.org/10.1016/0377-0273(78)90002-1.

Stamm, N., and Schmidt, M.W., 2017, Asthenospheric kimberlites: Volatile contents and bulk compositions at 7 GPa: Earth and Planetary Science Letters, v. 474, p. 309–321, https://doi.org/10.1016/j.epsl.2017.06.037.

Stubley, M.P., and Irwin, D., 2019, Bedrock Geology of the Slave Craton, Northwest Territories and Nunavut: Yellowknife, Canada, Northwest Territories Geological Survey, NWT Open 326 File 2019-01, https://www.arcgis.com/apps/mapviewer/index.html?layers=02cf96d56f0f4c98824f18809fab7ca1

Torsvik, T.H., Burke, K., Steinberger, B., Webb, S.J., and Ashwal, L.D., 2010, Diamonds sampled by plumes from the core–mantle boundary: Nature, v. 466, p. 352–355, https://doi.org/10.1038/nature09216.

Vuilleumier, R., Seitsonen, A.P., Sator, N., and Guillot, B., 2015, Carbon dioxide in silicate melts at upper mantle conditions: Insights from atomistic simulations: Chemical Geology, v. 418, p. 77–88, https://doi.org/10.1016/j.chemgeo.2015.02.027.

Watson, E.B., 1982, Melt infiltration and magma evolution: Geology, v. 10, p. 236–240, https://doi.org/10.1130/0091-7613(1982)10<236:MIAME>2.0.CO;2.

Zhang, Y., Ni, H., and Chen, Y., 2010, Diffusion data in silicate melts: Reviews in Mineralogy and Geochemistry, v. 72, p. 311–408, https://doi.org/10.2138/rmg.2010.72.8.

SUPPLEMENTAL MATERIALS

Selection of Jericho kimberlite as a starting melt

The starting melt composition used in this study is based on the hypabyssal Jericho kimberlite (Kopylova et al., 2007), from which the proto–kimberlite melt was reconstructed prior to orthopyroxene assimilation (Table S1). This composition overlaps with other near–primary kimberlite melts (Stamm and Schmidt, 2017) and falls within the broader compositional ranges reported in recent literature (Giuliani et al., 2023). Although averaging major element compositions from the dataset of Dalton et al. (2024) was considered, the resulting average composition lacks geological context and does not correspond to any specific natural sample. As such, it provides limited utility for interpreting the behavior of real systems and complicates direct comparison with observed samples. The use of a single, well–characterized natural melt composition preserves geological relevance and enables a direct link to the known tectonic setting of the Slave craton.

Atomic self–diffusion

Trajectories and thermodynamic parameters of each snapshot are extracted from the OUTCAR files generated by VASP. Mean squared displacements of the atoms are computed as a function of time. Two transport regimes are distinguished: the initial phase, spanning from 0 to less than 500 fs, represents the ballistic regime and exhibits a steeper slope than the subsequent phase, which corresponds to diffusive motion. When calculating diffusivity, the first 500 fs are excluded, and the slope of the diffusive regime is used. A linear regression fit to the diffusive portion of the mean squared displacement curves yields the self–diffusion coefficients for each element. Pressure as a function of density and temperature is directly computed by VASP, with a thermal correction applied at all conditions to account for the kinetic energy of the atoms.

Table S1: Chemical compositions of the Jericho kimberlite, the renormalized composition without volatiles, and the theoretical dry kimberlite melt. All numbers are reported in weight percent (wt%). The first column is a reconstruction of primitive melts at depth, prior to orthopyroxene assimilation, based on Kopylova et al. (2007). The second column shows the same composition, renormalized to 100% after removing volatiles and components present in low abundance. The third column reports the calculated oxide wt% of the theoretical model. The difference between the second and third columns reflects the deviation between the target bulk composition (Kopylova et al. 2007) and the composition used in the simulation cell.

Oxide (wt %)	Jericho kimberlite	Renormalized Jericho kimberlite	Dry kimberlite, this study
SiO_2	26.70	33.38	33.25
TiO_2	1.73	2.16	2.68
Al_2O_3	1.57	1.96	1.71
Cr_2O_3	0.36		
FeO total	7.58	9.48	9.64
MnO	0.18		
MgO	28.25	35.32	35.15
CaO	12.90	16.13	15.99
Na_2O	0.10		
K_2O	1.26	1.58	1.58
P_2O_5	0.10		
CO_2	9.88		
H_2O	9.07		
Total	98.94	100	100

Self–diffusion coefficients of all atomic species are shown in Figure S2. When fewer than three atoms of a given species are present, the statistics are insufficient, as shown by the increased scatter for titanium, aluminum, and potassium atoms. While the 1500 K isotherms generally follow the trends at higher isotherms, possible discrepancies are due to the kimberlites being an undercooled melt at this low temperature.

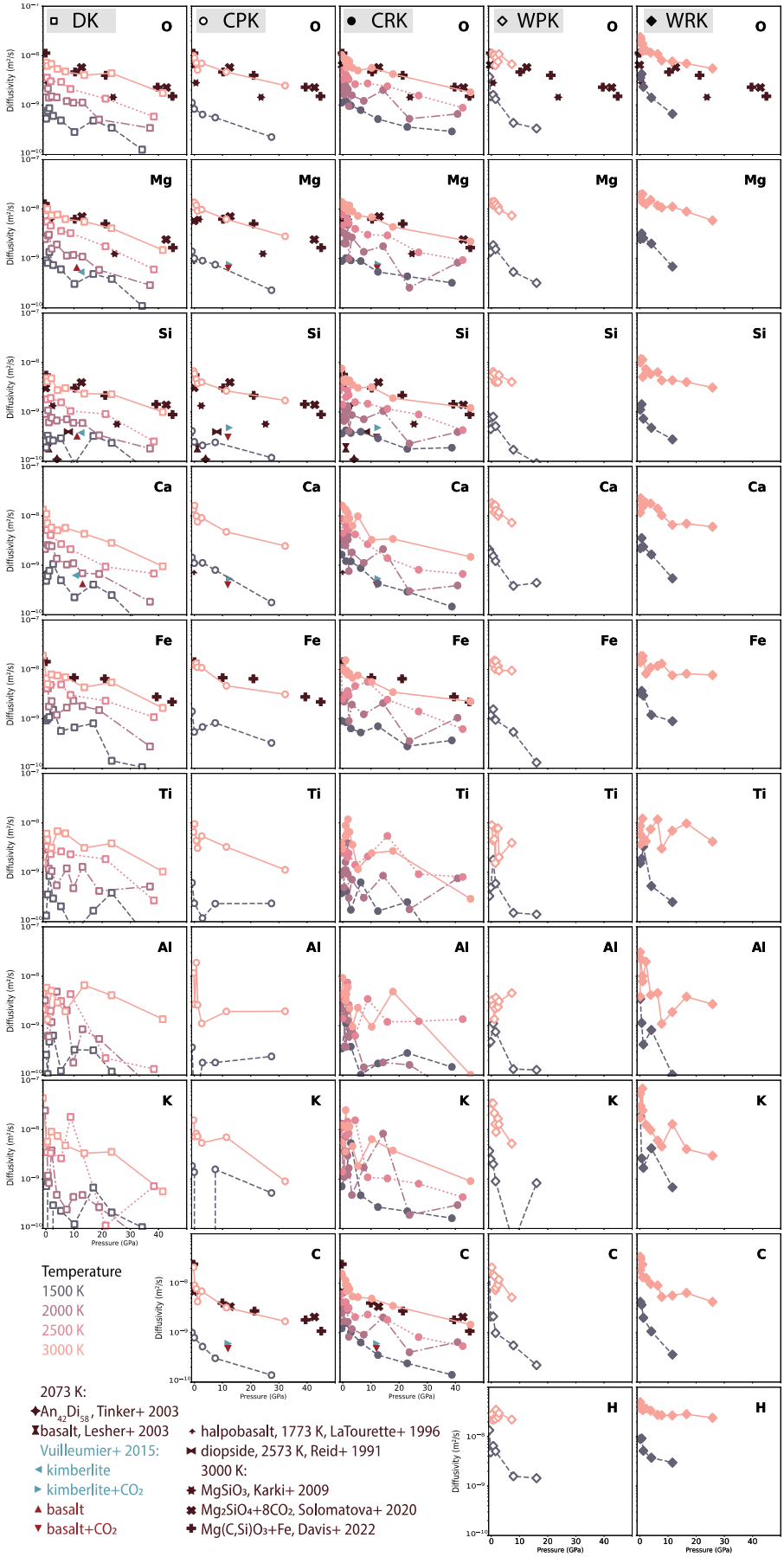

Figure S2. Self-diffusion coefficients versus pressure for kimberlite compositions with different volatile contents, compared with literature values for silicate melts at similar temperatures. DK—dry kimberlite; CPK—carbon-poor kimberlite; CRK—carbon-rich kimberlite; WPK—water-poor kimberlite; WRK—water-rich kimberlite.

Equation of state (EOS)

Pressure and density values of kimberlite melts are used to fit a third-order Birch–Murnaghan EOS (Fig. S3 and Fig. S4):

$$P(\rho) = \frac{3}{2}K_0\left[\left(\frac{\rho}{\rho_0}\right)^{\frac{7}{3}} - \left(\frac{\rho}{\rho_0}\right)^{\frac{5}{3}}\right]\left[1 + \frac{3}{4}(K_0' - 4)\left(\left(\frac{\rho}{\rho_0}\right)^{\frac{2}{3}} - 1\right)\right]$$

where P is pressure, K_0 is the bulk modulus, ρ is density, ρ_0 is the reference density, and K_0' is the derivative of the bulk modulus with respect to pressure.

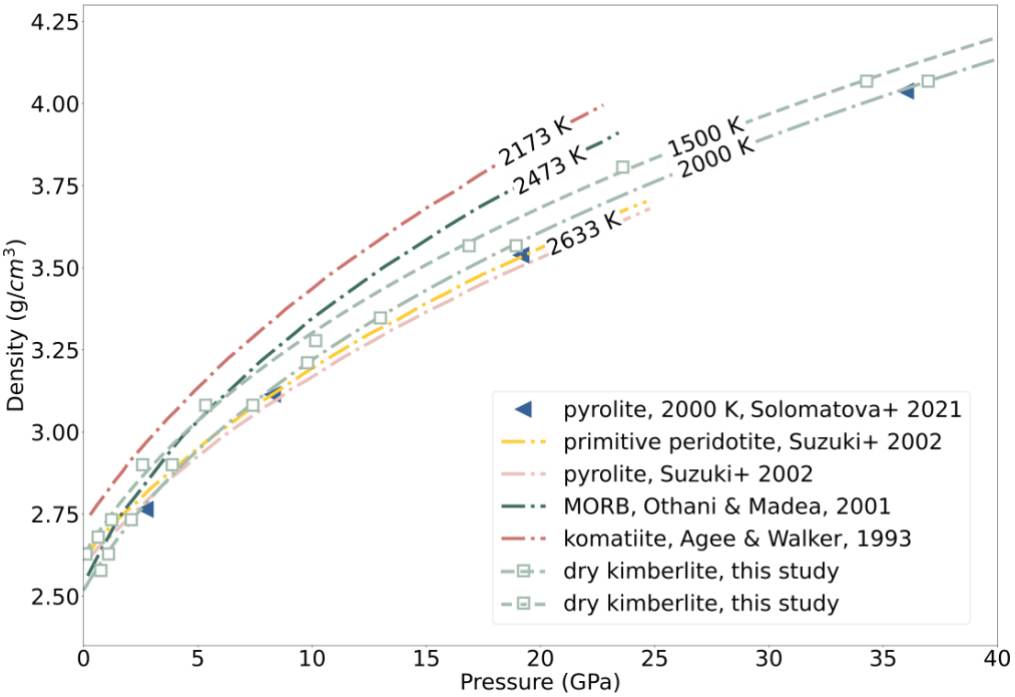

Figure S3. Density of dry kimberlite at 1500 K and 2000 K using Birch-Murnaghan equation of state, compared with experimental density measurements of various silicate melts at similar temperatures.

Comparison of the third-order Birch–Murnaghan EOS for kimberlite with experimental density data (Fig. S3) shows that dry kimberlite is less dense than komatiite (Agee and Walker, 1993) at 2000 K. MORB (Ohtani and Maeda, 2001) at 2473 K remains slightly denser than dry kimberlite at 2000 K. At higher pressures, primitive peridotite and pyrolite (Suzuki et al., 2002) at 2633 K exhibit densities comparable to, but slightly lower than, dry kimberlite. These comparisons show that the results fall within the range of experimentally measured melt densities.

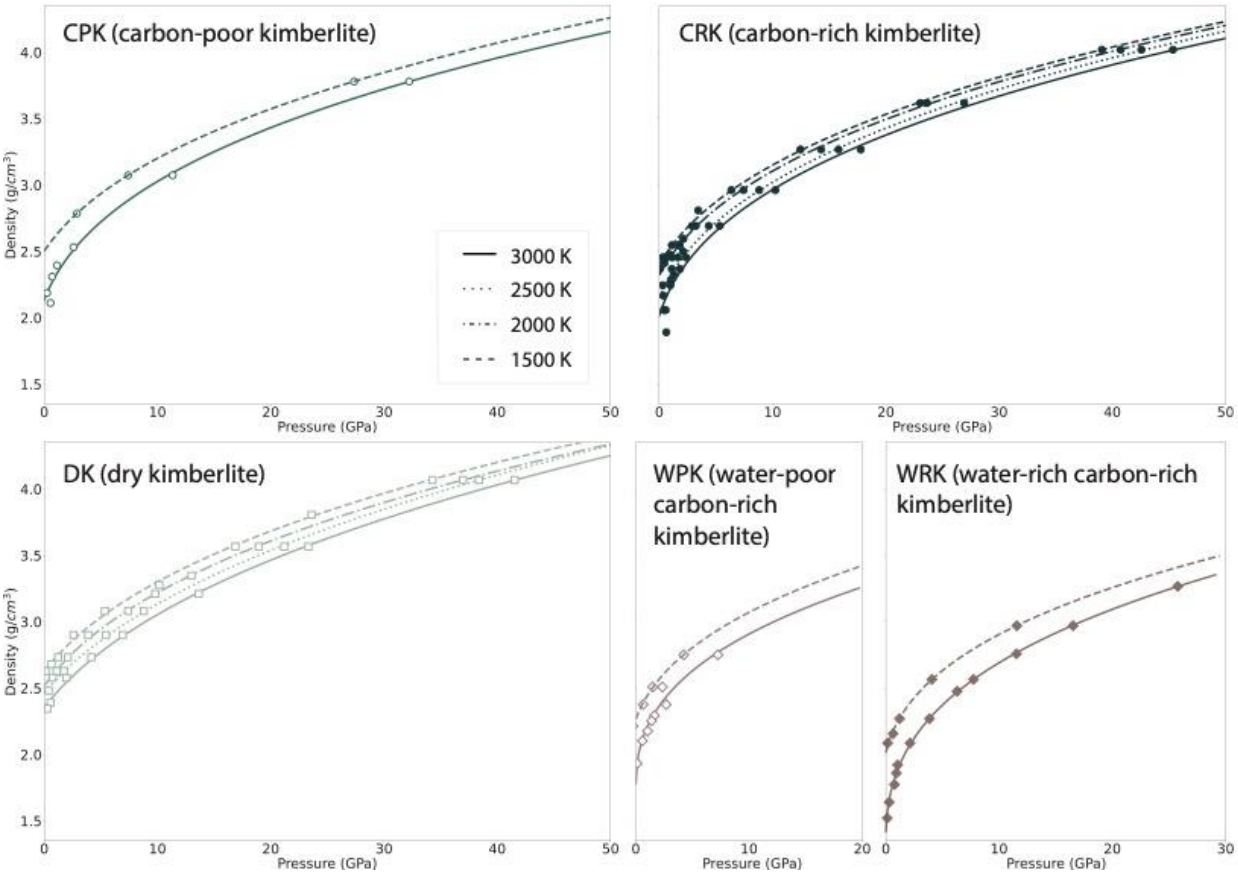

Figure S4. Each subplot shows Birch–Murnaghan equation of state (EOS) fits to all isotherms for the respective kimberlite melt compositions. Density increases with decreasing temperature, consistent across all datasets. Although the 1500 K isotherms fall within the undercooled melt regime at high pressures, both the EOS fits and the pressure–density data exhibit coherent and consistent trends.

The exact carbon content for neutral buoyancy of kimberlite melts relative to the Slave craton is determined by interpolating between the carbon contents of CPK (5.6 wt%) and CRK (11.3 wt%) at 1.2 GPa to find the value corresponding to the craton's density (Fig S5).

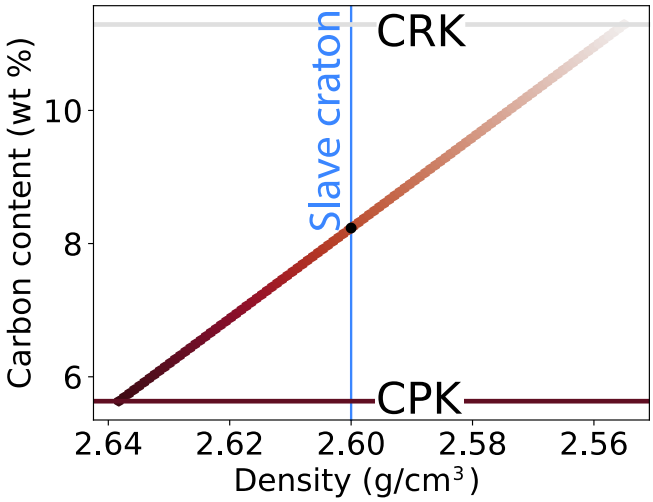

Figure S5. Carbon content in relation to density at 1.2 GPa. Interpolation between CPK and CRK identifies the carbon content corresponding to the Slave craton's density (2.6 g/cm^3). CPK—carbon-poor kimberlite; CRK—carbon-rich kimberlite.

Transport capacity

The volume fraction of entrained depleted peridotite (DPer) fragments that kimberlite melts can carry while remaining neutrally buoyant with respect to the Slave craton (Snyder, 2008) is calculated. A density profile of DPer (ρ_p) is used, derived along a 45 mW/m² geotherm from Faccincani et al. (2021). Intersection points are identified where the total density of the system (melt + crystals) equals the density of the Slave craton. The relationship between density (ρ), mass (m), and volume (V) is given by:

$$\rho = \frac{m}{V}$$

The total volume of the magma system (V_{total}) is the sum of the volumes of kimberlite and peridotite:

$$V_{total} = V_k + V_p$$

Volume of kimberlite melt (V_k) and DPer fragments (V_p) can be expressed as:

$$V_k = (1 - X)V_{total}$$

$$V_p = XV_{total}$$

The total density (ρ_{total}) is calculated as the ratio of total mass to total volume:

$$\rho_{total} = \frac{m_{total}}{V_{total}} = \frac{m_k + m_p}{V_{total}}$$

The densities ρ_k and ρ_p are given by:

$$\rho_{total} = \frac{\rho_k V_k + \rho_p V_p}{V_{total}}$$

Substituting V_k and V_p yields:

$$\rho_{total} = \frac{\rho_k (1 - X)V_{total} + \rho_p X V_{total}}{V_{total}}$$

Simplifying gives:

$$\rho_{total} = \rho_k (1 - X) + \rho_p X = \rho_k - X\rho_k + \rho_p X$$

Rearranging the equation to solve for X yields the following expression:

$$X = \frac{\rho_{total} - \rho_k}{\rho_p - \rho_k}$$

Model assumptions

While the simulations provide valuable constraints on the intrinsic properties of volatile–rich kimberlite melts, several modeling simplifications must be acknowledged. The model assumes that DPer is solid, chemically inert, and resistant to melting, allowing the transport properties of the melt to be isolated and the resulting estimates to be treated as an upper bound on transport capacity. In natural systems, however, assimilation of lithospheric mantle components can substantially alter melt composition, especially by increasing SiO_2 content and

promoting CO_2 exsolution, which would likely enhance melt buoyancy and ascent. This complexity is not captured in the model, which excludes the possibility of peridotite decomposition and reactive transport.

Although the simulation cells are too small to accommodate macroscopic bubble formation, nanobubble nucleation and the emergence of a CO_2-rich vapor phase are observed below 3 GPa. This vapor phase is included in the density calculations to reflect bulk melt behavior. The model does not account for xenolith disaggregation, which could further enhance melt acceleration through carbonate devolatilization at depth. Additionally, multi-pulse emplacement events and lithospheric preconditioning are important aspects of kimberlite magmatism but occur on spatial and temporal scales beyond the reach of atomistic simulations. Instead, the present approach focuses on local pressure–temperature–composition controls on diffusivity and density, providing a conservative yet physically grounded estimate of the volatile content required for buoyant ascent.

References

Agee, C. B., and Walker, D., 1993, Olivine flotation in mantle melt. Earth and Planetary Science Letters, v. 114(2-3), p. 315-324, https://doi.org/10.1016/0012-821X(93)90033-6.

Giuliani, A., Dalton, H., & Pearson, D. G., 2025, Kimberlites: The deepest geochemical probes of Earth. Treatise on Geochemistry (Third edition), p. 159-230, https://doi.org/10.1016/B978-0-323-99762-1.00064-4.

Faccincani, L., Faccini, B., Casetta, F., Mazzucchelli, M., Nestola, F., and Coltorti, M., 2021, EoS of mantle minerals coupled with composition and thermal state of the lithosphere: Inferring the density structure of peridotitic systems. Lithos, v. 404, p. 106483, https://doi.org/10.1016/j.lithos.2021.106483.

Giuliani, A., Schmidt, M. W., Torsvik, T. H., and Fedortchouk, Y., 2023, Genesis and evolution of kimberlites. Nature Reviews Earth & Environment, p. 1–16, https://doi.org/10.1038/s43017-023-00481-2.

Kopylova, M. G., Matveev, S., and Raudsepp, M., 2007, Searching for parental kimberlite melt. Geochimica et Cosmochimica Acta, v. 71(14), p. 3616-3629, https://doi.org/10.1016/j.gca.2007.05.009.

Ohtani, E., and Maeda, M., 2001, Density of basaltic melt at high pressure and stability of the melt at the base of the lower mantle. Earth and Planetary Science Letters, v. 193, p. 69-75, https://doi.org/10.1016/S0012-821X(01)00505-2.

Snyder, D. B., 2008, Stacked uppermost mantle layers within the Slave craton of NW Canada as defined by anisotropic seismic discontinuities. Tectonics, v. 27, https://doi.org/10.1029/2007TC002132.

Stamm, N., and Schmidt, M. W., 2017, Asthenospheric kimberlites: Volatile contents and bulk compositions at 7 GPa. Earth and Planetary Science Letters, v. 474, p. 309–321, https://doi.org/10.1016/j.epsl.2017.06.037.